Master thesis

A heterodyne laser distance metrology for NICE

Thomas Birbacher

Advisors

Adrian M. Glauser

Mohanakrishna Ranganathan

Sascha P. Quanz

Abstract

Context. The Nulling Interferometry Cryogenic Experiment (NICE) requires stabilization of the optical path lengths of the interferometer to within 0.45 nm peak-to-peak against vibrations, thermal expansion, and turbulence, for frequencies from 10 μHz (≈ 20 h) to 100 Hz.

Methods. A heterodyne differential laser distance metrology to track the optical path length change between two beams was designed, built, and characterized. The metrology operates with a HeNe laser at room pressure and temperature with a beat frequency of 10 kHz.

Results. The metrology has a bandwidth of 5 kHz and measurement noise of $\sigma = 96$ pm and 0.74 nm peak-to-peak over a period of 2 s. Over a period of 40 h, the metrology drifts by 3.5 nm, which is believed to be mostly caused by changes in air pressure and temperature in the laboratory.

Conclusion. The goal for NICE was not met by a factor of ≈ 1.5 regarding short-term noise, and a factor of ≈ 8 regarding long-term drift. The goal for bandwidth was met. Despite the drift over time, the metrology is a good candidate for further development, since it is limited by the uncontrolled environmental conditions in a large box, which can be improved with a better setup.

Contents

List of Symbols

s	optical path length
x, d, ℓ	length
ϕ	phase
f	frequency
n	index of refraction
c	speed of light in vacuum
T	temperature
P	pressure
I	intensity
t	time
δ	alignment correction factor
$\omega = 2\pi f$	angular frequency
$k = n\omega/c$	wavevector
$\lambda_0 = c/f$	wavelength in vacuum
$\lambda = c/(nf)$	wavelength in medium

1 Introduction

1.1 Context

It is one of the long-term goals of astronomy to find habitable worlds, or even life, on other planets. Currently, one promising approach is to analyse the chemical composition of atmospheres by means of spectroscopy.

Several experiments have been proposed to characterize the atmospheres of "earth-like" planets, one of them being the Large Interferometer For Exoplanets[7,18] (Life), a potential space mission which directly images the thermal emission of planets in the infrared, at $4\,\mu m$ to $18.5\,\mu m$, in order to characterize the chemical composition of their atmospheres.

Life is based on nulling interferometry to improve the planet-to-star contrast, and the nulling depth required to block the star out sufficiently is $\approx 10^{-6}$, which in turn requires accurate matching of the optical path lengths between the spacecraft.

In order to develop the technology required to achieve this contrast, and thus demonstrate the feasibility of such a mission, the Nulling Interferometry Cryogenic Experiment[10] (Nice) is currently being built, with the goal of demonstrating a null depth of 10^{-6} in the mid-infrared at cryogenic conditions and at stellar flux levels, in order to simulate the conditions of Life. Currently, the warm precursor of Nice is being built, which operates under standard atmospheric conditions.

Achieving such a null depth requires exact matching of the optical path lengths of the interferometer in order to destructively interfere a broadband infrared light source. The tentative requirements for Nice are a regulation of the optical path length to within $0.45\,nm$ peak-to-peak with a bandwidth of $100\,Hz$, over a period of $20\,h$. It is the aim of this work to design, build, and characterize a distance metrology that satisfies these requirements.

1.2 Requirements on the metrology

The requirements of Nice on the metrology are summarized in table 1.1, which are $0.45\,nm$ peak-to-peak noise over a time of $20\,h$ with a bandwidth of $100\,Hz$. However, a higher initial bandwidth of $1\,kHz$ is targeted in order to characterize higher-frequency vibrations within the Nice setup, even though this frequency range will probably not be used for active path length stabilization.

Parameter	Requirement
Peak-to-peak noise	0.45 nm
Bandwidth	1 kHz
Measurement time	20 h
Attenuation	$6 \cdot 10^5$

Table 1.1: Requirements and parameters of the metrology to achieve the goals of NICE.

The path of the metrology measurement beams through NICE is not yet fixed, but a tentative analysis yielded an attenuation of $\approx 6 \cdot 10^5$ of the laser beam intensity by the optical components. Thus, the metrology must be capable of measuring faint signals. To achieve this, the beat frequency of the heterodyne signal should be as low as possible, since lower bandwidth signals are easier to measure for a given signal-to-noise ratio. Since vibrations of 1 kHz should be measurable, a beat frequency of 10 kHz was selected, which provides some overhead.

Given the low beat frequency, coupling the light into optical fibres for parts of the setup would be problematic, since acoustic noise can couple into the fibres. This would would require active components to measure and clean up the phase of the laser beam after leaving the fibre,[20] which was avoided to reduce complexity.

1.3 Other work

The interferometer section of the metrology in this work is based on an article by Joo,[11] which is part of the master thesis by Clark.[6] Their metrology is capable of measuring at sub-nanometre resolution, with a standard deviation of 0.028 nm over a 10 s period when sampling at 500 Hz. They performed 12 h drift measurements and found a thermal coupling coefficient of $5.5 \, \mathrm{nm \, K^{-1}}$. Furthermore, their setup is compact and does not require many components, and was measured to have a good rejection of common mode path length changes within the metrology. However, it is fibre coupled, which would be too noisy for the low beat frequency that is required for NICE, so no optical fibres are used in this work.

The frequency splitting in this work is based on Schuldt's[20] metrology, but again without coupling the beams into optical fibres.

The goal of this work is to improve upon the results of the above authors by increasing the sampling rate of the distance to 10 kHz, and by measuring the drift of the metrology over longer time periods and multiple temperature cycles.

1.4 Outline

Chapter 2 contains a theoretical description of differential heterodyne interferometry, and a derivation of the requirements on the system to achieve the goals of NICE.

Chapter 3 describes the experimental setup and derives the estimated uncertainty of the measurements.

Chapter 4 contains the results of the measurements and discusses them briefly.

Chapter 5 summarizes the results, and compares them with the theoretical model of the metrology and the requirements for NICE. Potential improvements to the setup are also presented.

2 Theory

This chapter provides details on the theory of differential heterodyne interferometry, the requirements for the Nulling Interferometry Cryogenic Experiment (NICE), the working principle of an acousto-optic modulator (AOM), and gives an overview of the conventions used for the noise analysis.

In section 2.1, the relation between phase and distance in an electromagnetic wave, which is a fundamental equation for interferometry, is derived.

Section 2.2 derives the heterodyne principle, a method to recover the phase of a high-frequency signal by interfering it with a signal of similar frequency to create an easier to measure signal with low beat frequency. Together, sections 2.1 and 2.2 present a simplified model of heterodyne interferometry, which can be used as an introduction to the topic. They are not logically necessary to understand the rest of this work, but can be useful to provide some intuition.

Section 2.3 independently shows a more detailed model of the interferometer used in this work, and demonstrates how it is resistant to common mode changes in the optical path lengths. The main equation used for the data analysis is derived here.

Section 2.4 contains the derivation of the 0.45 nm accuracy requirement on the metrology for NICE.

Section 2.5 is an overview of the working principle of an acousto-optic modulator, which is used to shift the frequencies of the laser beam for the heterodyne interferometer.

Section 2.6 briefly describes the conventions used for the noise analysis, and in particular, the periodogram.

2.1   Interferometry

The derivation in this section shows how the phase of an electromagnetic wave in a medium changes with position. This is a fundamental equation for interferometry, since it can be used to relate the measured phase of an interference pattern between beams to the difference in optical path length between the beams. The result is also found in Schödel,[21] and is commonly used in interferometry, but I could not find a good derivation of the equation in the literature, so I am deriving it here.

An electromagnetic plane wave is described by

$$\boldsymbol{E}(\boldsymbol{r}, t, \phi) = \mathrm{Re}\left[\boldsymbol{E}_0 e^{i(\boldsymbol{k}\cdot\boldsymbol{r} - \omega t + \phi)}\right],$$

where $\boldsymbol{k}\cdot\boldsymbol{r} + \phi$ is the phase of the wave, and ϕ is a constant phase shift. When moving a distance Δx away from $\boldsymbol{r}$ in the positive x-direction, a phase shift $\Delta\phi$ occurs. To find this phase shift, we solve

$$\boldsymbol{E}(\boldsymbol{r} + \Delta x \boldsymbol{e}_x, t, 0) = \boldsymbol{E}(\boldsymbol{r}, t, \Delta\phi),$$
$$\implies \boldsymbol{k}\cdot(\boldsymbol{r} + \Delta x \boldsymbol{e}_x) - \omega t = \boldsymbol{k}\cdot\boldsymbol{r} - \omega t + \Delta\phi,$$

which yields

$$k_x \Delta x = \Delta\phi.$$

For an electromagnetic wave travelling in the x-direction in a medium with refractive index n, $k_x = n\omega/c$, where c is the speed of light in vacuum. We also use the optical path length $\Delta s = n\Delta x$. This gives

$$\Delta\phi = \frac{\omega}{c}\Delta s = \frac{2\pi\Delta x}{\lambda}. \tag{2.1}$$

Even though the derivation does not involve heterodyne interferometry, it is one of the main equations used in the data analysis. It is used to convert the phase of the beat signal of the interferometer to the optical path length difference between measurement mirrors. The justification for why this result can be used is in section 2.3, which shows a more detailed model of the metrology used in this work.

2.2   Heterodyne interferometry

The phase of an electromagnetic wave can be converted into a displacement with eq. (2.1). This section introduces the heterodyne principle, which is a method to measure the phase of a high-frequency signal, such as visible light, but only requiring measurement devices with much lower bandwidth than the signal frequency.

Heterodyne and homodyne interferometry.   With homodyne interferometry, two parallel plane waves with the same frequency, but different phase, interfere on a CCD or photodiode, and the phase difference between the beams can be calculated from the intensity of the interference, or from the fringe pattern that results from waves that are not exactly plane and parallel.

With heterodyne interferometry, the plane waves additionally differ slightly in frequency. The phase is obtained by measuring the beat signal that results from interfering two signals with different frequencies, and comparing the beat signal to a reference signal.

For both methods, the displacement can be calculated from the phase difference between the two signals with eq. (2.1).

One of the advantages of heterodyne interferometry over homodyne interferometry is that the distance information is encoded in the phase difference between two signals, rather than the intensity. The phase of a signal is more resistant to environmental noise – such as air turbulence or fluctuations of the laser output – than the intensity of the signal.

Derivation of the heterodyne principle. Let $E_1(t)$ and $E_2(t)$ be two sine waves with different frequencies and phase offset $\Delta\phi$:

$$E_1(t) = \sin(\omega_1 t + \Delta\phi),$$
$$E_2(t) = \sin(\omega_2 t).$$

If we assume that E_1 and E_2 correspond to the electric field strengths of two laser beams, then the intensity I_M of the combined beam that can be measured with a photodiode is

$$I_M(t) \propto [E_1(t) + E_2(t)]^2.$$

After some algebra, this yields

$$I_M(t) \propto + 1 - \frac{1}{2}\cos(2\omega_2 t) - \frac{1}{2}\cos(2\omega_1 t + 2\Delta\phi)$$
$$- \cos[(\omega_1 + \omega_2)t + \Delta\phi] + \cos[(\omega_1 - \omega_2)t + \Delta\phi].$$

Assume that $\omega_1 \approx \omega_2 \gg \|\omega_1 - \omega_2\|$. Then the right side of the above equation can be split into three terms, depending on their frequency.
- The term $\propto 1$ is constant, and called the DC term.
- The terms $\cos(2\omega_2 t)$, $\cos(2\omega_1 t)$, and $\cos[(\omega_1 + \omega_2)t]$ are called the high-frequency (HF) terms.
- The term $\cos[(\omega_1 - \omega_2)t]$ is called the intermediate-frequency (IF) term.

The HF terms are in the range of 1000 THz for red light, which is outside the bandwidth of a photodiode, so these terms are discarded. The DC term can be discarded with a high pass filter. The IF term for the metrology in this work is 10 kHz, and is measured with a photodiode and an oscilloscope.

To recover the phase ϕ from the IF term, the intensity I_M is compared with a reference signal $I_R(t) = \cos[(\omega_1 - \omega_2)t]$. The phase can then be measured with an electronic phase detector.

With eq. (2.1), the optical path length difference can then be calculated from the measured phase.

2.3 Differential heterodyne interferometry

The heterodyne interferometer used in the metrology in this work has the additional property of being differential, meaning that two measurement beams

7

(M_1 and M_2) and two reference beams (R_1 and R_2) are used. The measurement beams both have frequency ω_1, which is slightly shifted from the frequency ω_2 of the reference beams. The combined beams $M_1 + R_1$ and $M_2 + R_2$ are measured with separate photodiodes, and the phase difference between the signal from the photodiodes is used to calculate the optical path length difference (OPD) between the two measurement beams. As will be shown in this section, the advantage of this method is that the metrology is resistant to changes in the optical path length (OPL) that are common mode to multiple beams.

The exact setup of the metrology in this work is shown in fig. 3.1 in the next chapter, which can be referred to for easier visualization, but the model in this section applies to differential heterodyne interferometers in general.

The optical path length of the beams in the metrology is divided into four segments:

- s_{cm}, the OPL that is common to all beams, or common mode OPL,
- s_m, the OPL that is common to the two measurement beams
- s_r, the OPL that is common to the two reference beams, and
- s_1 and s_2, the OPLs that are unique to the left measurement beam and the right measurement beam.

The optical path length difference to be measured is the difference $\Delta s = s_1 - s_2$.

The electric field of each of the four beams on the photodiode can be expressed as

$$
\begin{aligned}
M_1(t) &\propto \sin[\omega_1/c(s_{cm} + s_m + s_1) - \omega_1 t], \\
M_2(t) &\propto \sin[\omega_1/c(s_{cm} + s_m + s_2) - \omega_1 t], \\
R_1(t) &\propto \sin[\omega_2/c(s_{cm} + s_r) - \omega_2 t], \\
R_2(t) &\propto \sin[\omega_2/c(s_{cm} + s_r) - \omega_2 t].
\end{aligned}
\tag{2.2}
$$

The intensity I_n at photodiode n is proportional to $(M_n + R_n)^2$, which after some algebra gives

$$
\begin{aligned}
I_1 &\propto DC + HF + \cos\left[\frac{\omega_1}{c}(s_{cm} + s_m + s_1) + \frac{\omega_2}{c}(s_{cm} + s_r) + (\omega_1 - \omega_2)t\right], \\
I_2 &\propto DC + HF + \cos\left[\frac{\omega_1}{c}(s_{cm} + s_m + s_2) + \frac{\omega_2}{c}(s_{cm} + s_r) + (\omega_1 - \omega_2)t\right].
\end{aligned}
$$

The DC term is discarded with a high-pass filter, and the HF term is discarded by the bandwidth of the photodiode. The phase difference between the IF terms of I_1 and I_2 is

$$
\Delta\phi = \frac{\omega_1}{c}(s_1 - s_2),
\tag{2.3}
$$

which gives the optical path length difference as a function of the phase difference between the beat signals. Note that this is similar to the result in eq. (2.1).

The differential heterodyne measurement shown here has the advantage of rejecting s_{cm}, s_m, and s_r. This is necessary, because the thermal expansion

coefficient of the steel or aluminium[4] surface of an optical table is $\approx 2 \cdot 10^{-5}\,\mathrm{K}^{-1}$, and a setup with a length of $50\,\mathrm{cm}$ expands by $10\,\mathrm{\mu m\,K}^{-1}$. This would make nanometre distance measurements impossible.

Rearranging eq. (2.3) yields

$$\Delta x = \frac{c}{2n\pi f}\Delta\phi,$$

which is the measured path length difference between the two measurement beams as a function of phase. Since the phase measurement is limited to $\Delta\phi \in [0, 2\pi)$, the absolute value of the path length difference cannot be determined. For practical measurements, a zero point is required, which in the case of NICE will probably be determined without this metrology. For this work, it is assumed that the metrology is in a position of known x as a reference point when an experiment is started, and the Δ's will be dropped for a more convenient notation.

Since a movement of a measurement mirror by d in a direction perpendicular to the beam results in a length change of $x = 2d$ of the beam, the equation has to be corrected by a factor 2. Additionally, to account for misalignment between optical components, a correction factor δ is introduced. The final equation used for data analysis is thus

$$d = \frac{c}{4\pi}\frac{\phi\delta}{nf}. \tag{2.4}$$

2.4 Derivation of NICE requirements

The goal of the Nulling interferometry cryogenic experiment (NICE) is to achieve a null depth of 10^{-6}. In this section, the resulting requirement on the matching of the optical path lengths is derived.

Assume that two electromagnetic waves with equal amplitude E_0 and phase difference $\Delta\phi$ interfere destructively. The electric fields of the waves are

$$E_1(t) = E_0 \sin\left(\omega t + \Delta\phi\right),$$
$$E_2(t) = E_0 \sin(\omega t),$$

and the intensity of the null is $I_+ = (E_1 - E_2)^2/Z_0$, where Z_0 is the impedance of free space. The average intensity I_{avg} of the null signal is equal to the integral of the intensity over one period $T = 2\pi/\omega$, which evaluates to

$$I_{\mathrm{avg}} = \frac{1}{T}\int_0^T I_+(t)\,\mathrm{d}t = 2I_0 \sin\left(\frac{\Delta\phi}{2}\right)^2, \tag{2.5}$$

with $I_0 = E_0^2/Z_0$. The null contrast N is defined as $N = I_{\mathrm{avg}}/I_0$. Assuming a contrast $0 < N < 1$, solving eq. (2.5) for $\Delta\phi$ yields

$$\Delta\phi = 2\arcsin\left(\sqrt{N/2}\right) = \sqrt{2N} + O(N^{3/2}),$$

or expressed in terms of length Δx with eq. (2.1),

$$\Delta x = \frac{\lambda}{\pi} \arcsin\left(\sqrt{N/2}\right) = \frac{\lambda}{\pi}\sqrt{\frac{N}{2}} + O(N^{3/2}).$$

This constraint on the null depth agrees with the result of a more detailed derivation from Serabyn[22] up to a factor of $\sqrt{2}$.

For a wavelength of $\lambda = 10\,\mu$m and a null contrast of $N = 10^{-6}$, this yields $\Delta x_{\max} \approx 2.25$ nm. In order to account for other sources of error in the setup, a factor of uncertainty of 10 is used, which reduces the limit to $\Delta x_{\max} = 0.225$ nm.

Thus, in order to achieve the null contrast, the optical path length deviation Δx must be within $\pm\Delta x_{\max}$, which is a peak-to-peak deviation of 0.45 nm.

2.5 Acousto-optic modulators

An acousto-optic modulator (AOM) is a device that can change properties of monochromatic light – such as phase,[14] wavelength, direction, and intensity – by applying acoustic vibrations to the medium that the light travels through. This section follows the description by Pierce.[17]

AOMs are based on the acousto-optic effect, whereby a stress applied to an acousto-optic medium causes a change in the index of refraction.[13] An acoustic wave, consisting of regions of compression and expansion of the medium, thus produces a traveling diffraction grating from which light can be scattered.

Working principle. The scattering of light by acoustic waves in a medium was discovered experimentally by Debye[8] and Lucas,[15] and explained theoretically in a series of papers by Raman.[19] There are two analytical limits of the general model by Raman: Raman-Nath scattering and Bragg scattering.

For the metrology, AOMs are used as frequency shifters, which operate in the Bragg regime, shown in fig. 2.1. Laser light with angular frequency ω_1 and wavelength λ_1 enters the AOM at an angle θ to the surface normal of the AOM. An acoustic wave with angular frequency ω_s and wavelength λ_s creates a travelling diffraction grating of varying refractive index through the acousto-optic effect. Part of the laser beam passes straight through the AOM, which is called the zeroth order beam, and part of it is deflected by an angle of 2θ according to the Bragg condition,[3]

$$m\lambda_1 = 2\lambda_s \sin\theta, \tag{2.6}$$

where m is the order of diffraction. The efficiency of diffraction of light into a particular mode is controlled by adjusting the angle θ. Additionally, the frequency of the laser beam is shifted to $\omega_2 = \omega_1 + m\omega_s$. The frequency of the laser beam can thus be adjusted by changing the acoustic frequency ω_s. Typical values for ω_s are in the 100 MHz region, and depend on the mechanical properties of the medium.
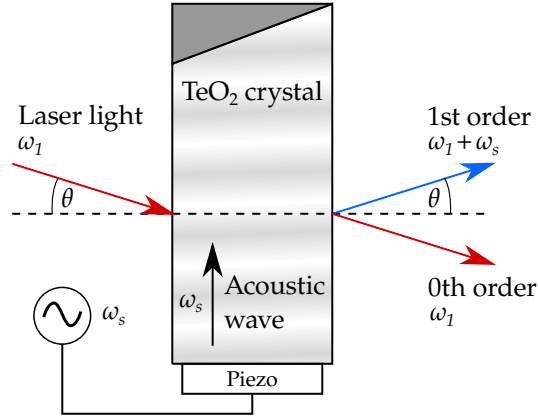
Figure 2.1: Setup of the acousto-optic modulator as a frequency shifter. The laser light coming from the left with angular frequency ω_1 is shifted by the angular frequency ω_s of the acoustic wave in the AOM. The acoustic wave is generated by a piezo actuator.

Photon-phonon interaction. The frequency-shifting action of an AOM can also be described by the scattering of a photon with a phonon, a quasi-particle of lattice vibrations in a crystal. Let $p_1 = (\hbar\omega_1, \hbar\boldsymbol{k}_1)$ be the four-momentum of a photon that enters the AOM, and $p_s = (\hbar\omega_s, \hbar\boldsymbol{k}_s)$ the quasi four-momentum[12] of the phonon that the photon interacts with. Because of conservation of energy, the momentum of the photon p_2 that results from this interaction obeys $p_1 \pm p_s = p_2$, and thus

$$\omega_1 \pm \omega_s = \omega_2, \tag{2.7}$$

$$\boldsymbol{k}_1 \pm \boldsymbol{k}_s = \boldsymbol{k}_2. \tag{2.8}$$

Equation (2.7) describes how the frequency of the photon is shifted up or down by f_s. Equation (2.8) describes how the direction of the photon changes, and for $\boldsymbol{k}_1$ perpendicular to $\boldsymbol{k}_s$, as in fig. 2.1, this results in $\tan(2\theta) = \lambda_1/\lambda_s$. While this is not identical with the Bragg condition (2.6), they agree for small λ_1/λ_s up to $O[(\lambda_1/\lambda_s)^3]$. Since in practice in an AOM, $\lambda_1/\lambda_s \ll 1$, the models agree reasonably well.[*]

2.6   Spectral analysis

When specifying the noise performance of a metrology, the contribution of noise from different frequency bins to the total noise is a concept of interest. This concept can be described by multiple quantities, such as the power spectrum, the power spectral density, the Fourier transform, and the periodogram. Since

---

[*]In this work, the medium of the AOM is TeO_2 with a speed of sound of $4.26\,\mathrm{km\,s^{-1}}$. The acoustic frequency is $f_s = 80\,\mathrm{MHz}$, and the laser wavelength is $\lambda_1 = 633\,\mathrm{nm}$. This results in $\lambda_1/\lambda_s \approx 0.012$.

Quantity	Description
N	number of samples
n	$\in \{0, 1, \ldots, N-1\}$
k	$\in \{0, 1, \ldots, N-1\}$
T	sampling period
$t_n = nT$	nth sampling instant
$x(t_n) = x_n$	input signal amplitude at time t_n
$\omega_k = k\Omega$	kth frequency sample
$\Omega = 2\pi/(NT)$	
$f_s = 1/T$	sampling rate

Table 2.1: Quantities used in the discrete spectral analysis.

multiple common definitions of these quantities exist, the conventions used in this work are briefly described.

Discrete Fourier transform. The definition of the discrete Fourier transform (DFT) used in this work is

$$\text{DFT}(\omega_k) = \sum_{n=0}^{N-1} x_n e^{-i\omega_k t_n},$$

with the definitions in table 2.1.

The quantity x_n will have the same unit as length throughout this work.

Sample variance. The sample variance $\hat{\sigma}^2$ is

$$\hat{\sigma}^2 = \frac{1}{N-1} \sum_{n=0}^{N-1} |x_n - \hat{\mu}|^2,$$

where $\hat{\mu} = 1/N \sum_{n=0}^{N-1} x_n$ is the sample mean. In this work, all data points used in the statistical analysis are mean-subtracted, so that $x_n - \hat{\mu}$ is used instead of x_n, which simplifies the sample variance to

$$\hat{\sigma}^2 = \frac{1}{N-1} \sum_{n=0}^{N-1} |x_n|^2.$$

This is useful when integrating the periodogram to obtain the variance with Parseval's theorem.

Periodogram. The periodogram is commonly defined as

$$P(\omega_k) = \frac{1}{N^2} |\text{DFT}(\omega_k)|^2,$$

and for a quantity x_n with units nm, the periodogram has units of nm^2.

To make plots easier to read and compare, independent of the sampling rate used in the measurement, this work instead uses the periodogram density,

$$\mathcal{P}(\omega_k) = \sqrt{\frac{P(\omega_k)}{f_s}},$$

in all plots and equations. The periodogram density has units $\text{nm}\,\text{Hz}^{-1/2}$. This is the same convention that the Python module `scipy.signal.periodogram` uses.

Parseval's theorem. Parseval's theorem[16] relates the periodogram to the sample variance of a time series. In the discrete case, it states that

$$\frac{1}{N} \sum_{n=0}^{N-1} |x_n|^2 = \sum_{k=0}^{N-1} P(\omega_k) \approx \int_{f_{\min}=1/T}^{f_{\max}=2f_s} \mathcal{P}(f)\,\mathrm{d}f, \qquad (2.9)$$

where the expression on the right is approximated with a numerical trapezoid integral. Since all samples are mean subtracted, and assuming $N \approx N - 1$, eq. (2.9) is equal to the sample variance $\hat{\sigma}^2$. This result can be used to calculate the contribution of noise with different frequencies to the total noise of the signal. The notation

$$\hat{\sigma}(f_1, f_2) = \sqrt{\int_{f_1}^{f_2} \mathcal{P}(f)\,\mathrm{d}f} \qquad (2.10)$$

is used to denote the contribution of noise from f_1 to f_2 to the total standard deviation of the signal.

Integrated noise. When measuring a signal for a time τ with sampling rate f_s, and discarding all signals with a frequency higher than f_s with a brick-wall low-pass filter, the expected standard deviation of the measured signal is

$$\hat{\sigma}(1/\tau, f_s) = \sqrt{\int_{1/\tau}^{f_s} \mathcal{P}(f)^2\,\mathrm{d}f}. \qquad (2.11)$$

This is useful to simulate the noise of measurements with a lowered sampling rate from a periodogram.

3 Experimental setup

This chapter provides a description of the metrology setup and the noise sources that are expected in the measurement.

Section 3.1 contains a detailed description of the optical setup of the metrology.

Section 3.2 contains an estimation of the sources of uncertainty that contribute to the metrology measurement, and describes which of these are expected to be dominant sources of error.

Section 3.3 describes the the raytracer that was programmed to simulate the setup, and shows the results of simulations that determine how sensitive the metrology is expected to be to thermal expansion of the optical table.

Section 3.4 contains the description and characterization of the photodiode amplifier that was built.

3.1   Overview

The setup of the metrology is shown in fig. 3.1, and consists of four parts: The laser source, the frequency splitting with acousto-optic modulators (AOMs), the metrology section around polarizing beam splitter PBS1, and the beam combiner BS3 with the photodiodes.

A frequency-stabilised HeNe laser generates a polarized beam that goes into an optical isolator to avoid backscattering, which could disturb the frequency stabilisation of the laser. The beam is split by BS1 into a measurement beam and a reference beam, which are shown as red and blue in the diagram. The measurement beam is frequency shifted by $f_1 = 80.00\,\text{MHz}$ by the acousto-optic modulator AOM1, and the reference beam is shifted by $f_2 = 79.99\,\text{MHz}$ by AOM2. The frequency difference between the two beams is then $\Delta f = f_1 - f_2 = 10\,\text{kHz}$, which is the beat frequency of the metrology. The two signals come from the same clock in a dual channel signal generator, such that the signals are mutually coherent. The reference beam is redirected by M3 and M4 such that it runs parallel to the measurement beam, but 1 cm lower.

The next section is also shown in fig. 3.2 in a three-dimensional view, since the beams move vertically. The measurement beam on top and the reference beam on the bottom enter BS2, which is used to split both beams horizontally.

They both pass straight through the polarizing beam splitter PBS1, since they are both polarized vertically, in the pass direction of the PBS. They both

15
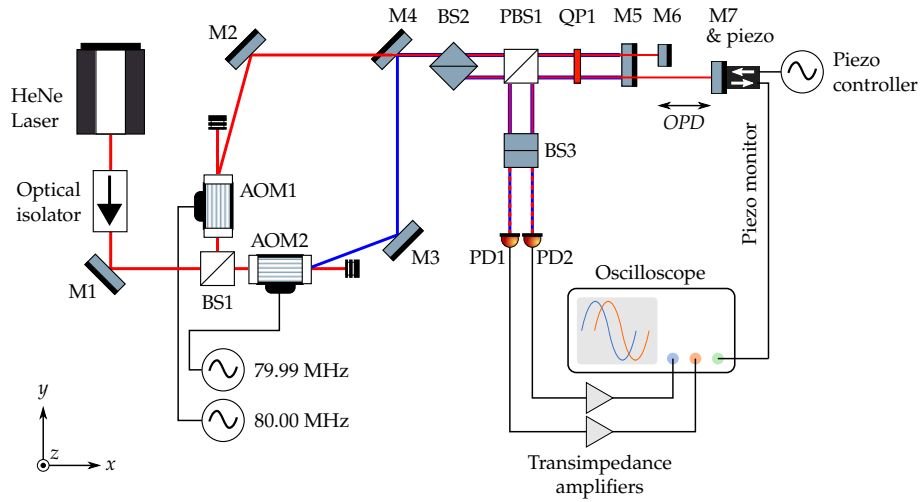
Figure 3.1: Diagram of the metrology setup.
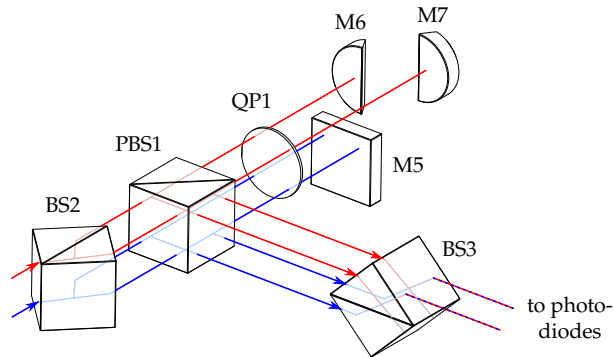
Figure 3.2: Detailed view of the interferometer section of the metrology. The beams coming from the AOMs (from the right) have frequencies that differ by 10 kHz, which is represented by a different colour. They are both are vertically polarized, so they pass the polarizing beam splitter PBS1. They pass a quarter wave plate QWP1, are reflected, and pass QWP1 again, which changes their polarization to horizontal. They are reflected from PBS1, and finally recombine behind BS3, from where they continue to the photodiodes.

pass a quarter wave plate QWP1 at an angle of 45° to the fast axis, after which the beams are circularly polarized. Both reference beams are reflected by M5, and the two measurement beams continue to M6 and M7. The metrology measures the optical path length difference (OPD) between M6 and M7, which are positioned a few centimetres from M5.

After reflection from the mirrors, all beams pass QWP1 again, which changes the polarization to horizontal, since passing a QWP twice acts like a half-wave plate. The beams are then reflected in PBS1 and are combined in BS3. BS3 gives four output beams, but only the upper two are recorded on photodiodes PD1 and PD2.

The measurement and reference beams are modelled with eq. (2.2). The photodiode signals contain a DC component that is discarded, a high frequency ($f_1 + f_2 \approx 1000$ THz) component that cannot be recorded, and an intermediate frequency component with frequency $f_1 - f_2 = 10$ kHz, which is the beat frequency. The phase difference between the two intermediate frequency sine waves is recorded on an oscilloscope, and the distance between M5 and M6 is calculated with eq. (2.3).

In some experiments, a calibrated closed-loop piezo stage is used to give a known displacement to the metrology and compare the distance measurement from the piezo and the metrology. For this purpose, the piezo monitor signal is also connected to the oscilloscope.

The configuration of the experiment where the reference mirror M5 and two measurement mirrors M6 and M7 are all used is called the three-mirror setup.

For characterization of the stability of the metrology, the reference mirror M5 is elevated such that all four beams are reflected by it, and M6 and M7 are removed. This configuration is called the one-mirror setup.

The setup was enclosed in a cardboard box to reduce disturbances by air currents and turbulence.

3.2 Noise analysis

The equation used for data analysis is eq. (2.4), and the estimation of the system noise is also based on this equation. The optical path difference d determined by the metrology in this model depends on the refractive index of air n, the frequency of the laser f, the alignment correction factor δ, and the phase measured by the phase detector ϕ.

To obtain an intuitive overview of the contributions of different noise sources to the total uncertainty in the measurement, this section gives a quick estimation based on linear Gaussian error propagation. While this method does not give precise results, since variables like temperature and pressure are not accurately described by normal distributions, it gives an order-of-magnitude estimate of the effects. As will be shown, most sources of error are not known accurately enough to warrant an approach with different probability distributions.

17

Quantity	Uncertainty or value
Laser frequency	$u_f/f \approx 6 \cdot 10^{-9}$
Index of refraction	$u_n/n \approx 4 \cdot 10^{-6}$
Alignment factor	not modelled
Measured phase	$u_\phi = 0.022\,\text{nm}$
OPD	$d \approx 1\,\text{mm to } 10\,\text{mm}$
Total system	$u_d \approx 4\,\text{nm to } 40\,\text{nm drift}$
	$u_d \approx 0.022\,\text{nm fast noise}$

Table 3.1: Modelled uncertainties of the metrology setup. The system is expected to be limited by temperature and pressure fluctuations over periods of hours, and limited by the phase noise of the measurement electronics during short measurements of a few seconds.

Following the analysis from Schödel,[21] the relative uncertainty of the measured displacement in eq. (2.4) is approximated as

$$\frac{u_d}{d} = \sqrt{\left(\frac{u_n}{n}\right)^2 + \left(\frac{u_f}{f}\right)^2 + \left(\frac{u_\delta}{\delta}\right)^2 + \left(\frac{u_\phi}{\phi}\right)^2},$$

where u_x is the uncertainty in variable x, quantified by the standard deviation of the variable's Gaussian probability distribution. The variables are the measured OPD change d, the refractive index n, the laser frequency f, the alignment correction factor δ, and the measured phase ϕ.

The uncertainties are calculated in sections 3.2.1 to 3.2.4, and the results are summarized in table 3.1. The total uncertainty is expected to be limited by $u_d/d \approx 4 \cdot 10^{-6}$, caused by temperature and pressure fluctuations, and also limited by $u_d = 0.022\,\text{nm}$, caused by electronic noise in the amplifier. Depending on the optical path length difference d, either of the two contributions can be the dominating limitation.

Alignment of the components by hand will result in an OPD between $1\,\text{mm}$ to $10\,\text{mm}$ between the two measurement beams.* This means that $d \approx 1\,\text{mm}$ to $10\,\text{mm}$, and thus $u_d \approx 4\,\text{nm}$ to $40\,\text{nm}$, which is limited by temperature and pressure fluctuations.

3.2.1 Laser frequency

The thorlabs HRS015B stabilized HeNe laser is specified with a vacuum wavelength $\lambda_0 = 632.991\,\text{nm}$ and a bandwidth of $\pm 3\,\text{MHz}$ over a $3\,\text{h}$ period.[23] This yields a frequency of $473.612\,512\,7(30)\,\text{THz}$, and a relative uncertainty of $u_f/f \approx 6.3 \cdot 10^{-9}$.

---

*Note that the optical path length difference between beams before BS2 does not contribute to d, since the differential metrology setup is resistant to common-mode path length changes. Only the OPD after BS2 contributes, which is a short section where beams can realistically be matched to within a few millimetres.

3.2.2 Index of refraction

A comprehensive and accurate model of the refractive index of air is the Ciddor model,[5] but due to its complexity, it is not suitable for a quick analytic treatment. Instead, an estimate is made based on the simpler Lorentz-Lorenz model.

The Lorentz-Lorenz model[2] states that the refractive index of a homogeneous liquid such as air can be approximated as

$$A \approx \frac{RT}{P} \frac{n^2 - 1}{3},$$

where A is the average molar refractivity of the mixture, which is a constant, T is the temperature, and P is the pressure. Since $n \approx 1$, the linear approximation $n^2 \approx 2n - 1$ can be used. Solving for n yields

$$n(P, T) = 1 + (n_0 - 1) \frac{P}{P_0} \frac{T_0}{T},$$

where $n_0 - 1 = 2.71 \cdot 10^{-4}$ at $P_0 = 1013 \, \text{hPa}$ and $T_0 = 20\,°\text{C}$ was determined from the Ciddor model.

The uncertainty of n in this model is thus

$$\frac{u_n}{n} = (n_0 - 1) \sqrt{\left(\frac{u_P}{P}\right)^2 + \left(\frac{u_T}{T}\right)^2}.$$

An estimate of the conditions in the lab from a thermometer in the lab and a local weather station on Hönggerberg are $P \approx 950(10) \, \text{hPa}$, and $T \approx 25.0(2)\,°\text{C}$. This gives

$$\frac{u_P}{P} \approx 0.0098, \qquad \frac{u_T}{T} \approx 0.010, \qquad \frac{u_n}{n} \approx -3.8 \cdot 10^{-6}.$$

The uncertainty in the refractive index depends equally on pressure and temperature.

3.2.3 Alignment correction factor

The alignment correction factor accounts for all undesired changes in the measurement of ϕ that have to do with the alignment of the setup, which depends on the position and orientation of all optical components. This includes effects such as the thermal expansion of the optical table and components, the relaxation of stresses in the components and mounts over time or with changing environmental conditions, the drift of the pointing of the laser over time, the cosine errors due to misalignment between the device under test and the metrology beams, and the changes in the interference pattern caused by the misalignment of beams.

Some of these error sources are hard to access experimentally, since the effects tend occur over long timescales and are hard to separate from each other.

In section 3.3, a raytracer was used to determine how resilient the metrology is against small changes in position and orientation of the optical components. Both the one-mirror setup and the three-mirror setup have a sensitivity to displacement of less than $5 \cdot 10^{-6}\,\mathrm{nm\,nm^{-1}}$, and a sensitivity to rotation of less than $10\,\mathrm{nm\,\mu rad^{-1}}$ in all components, except for the measurement mirrors M6 and M7 and the photodiodes. With a thermal expansion coefficient of the optical table of $2 \cdot 10^{-5}\,\mathrm{K^{-1}}$ over a length of 50 cm, the expected influence on the measured distance is $0.05\,\mathrm{nm\,K^{-1}}$. This confirms, as already shown in section 2.3, that the setup is expected to be resilient against common-mode changes in optical path lengths, in particular those caused by thermal expansion of the table.

The way in which the components change their orientation as a function of temperature or time is not known, so no theoretical prediction can be made on u_δ, other than that a change of position of the components, such as due to thermal expansion of the table, is expected not to be a dominating contribution to the system error.

3.2.4 Measured phase

This section treats noise that originates anywhere from just before the laser beam hits a photodiode, to the phase difference that is measured by the phase detector. This includes the shot noise of the laser beam, the shot noise of the electric current from the photodiode, the dark current from the photodiode, the noise from the interaction of the photodiode junction capacitance with the input voltage noise of the photodiode amplifier, the noise directly generated by the photodiode amplifier, and the noise from the phase detector.

Laser shot noise. The shot noise of the laser beam is quantified with the signal-to-noise ratio,

$$\mathrm{SNR} = \sqrt{N} = \sqrt{\frac{P\Delta t}{hc/\lambda}},$$

where N is the number of photons incident on the photodiode within a time Δt, from a source with power P and wavelength λ. Even when pessimistically assuming an attenuation of 100 of the $P = 1\,\mathrm{mW}$ laser beam, and a sampling time of $\Delta t = 1\,\mathrm{\mu s}$, the signal-to-noise ratio is $\approx 6 \cdot 10^4$, which is far less than the electronic noise measured from the photodiode amplifier.

Photodiode noise. The thorlabs FD11A photodiode is specified by the manufacturer with a noise-equivalent power (NEP) of $4.2\,\mathrm{fW\,Hz^{-1/2}}$ and a dark current of less than 100 pA.

The NEP contributes an $\mathrm{SNR} = P/(\mathrm{NEP} \cdot \sqrt{f}) \approx 2 \cdot 10^6$, where $f = 1/\Delta t$ is the bandwidth of the measurement electronics.

The photocurrent contributes current shot noise with $\mathrm{SNR} = \sqrt{I/(2|q|f)}$, where $I \approx 10\,\mathrm{\mu A}$ is the photocurrent, and q is the charge of the electron. This

yields SNR $\approx 6 \cdot 10^4$. The current shot noise of the 100 pA dark current is negligible.

Electronic noise. The output voltage noise of the photodiode amplifier has an SNR $\approx 10^3$. The noise of the photodiode amplifier in combination with the oscilloscope, used as a phase detector, is $u_\phi = 0.022$ nm, which is measured in section 3.4. This is the dominant contribution to the phase noise.

3.3 Raytracing

A raytracer was programmed in `Python` to determine how resilient the metrology setup is against changes in position and orientation of the components. The program is based on the descriptions of polarization raytracing in Enfeldt's thesis,[9] and extended with all optical components that are necessary to simulate the metrology.

Description of the raytracer. The raytracer is based on geometric optics. An initial ray is launched from the laser, with preset parameters for intensity, polarization, frequency, and local refractive index. The polarization and intensity of each ray are modelled with the Stokes vector, and the interactions with surfaces are modelled with the Mueller matrix.[1]

Each ray is propagated until it intersects with an object, where the properties of reflected and refracted rays are calculated. The directions of refracted and reflected rays are calculated with Snell's law and the mirror law, and the intensity and polarization are calculated by multiplying the material's Mueller matrix with the ray's Stokes vector, after transforming into a common coordinate system. For media like glass, Fresnel's law is used to determine the Mueller matrix, and ideal polarizing beam splitters and quarter-wave plates are assumed for the other components.

A ray is propagated until it either reaches the maximum iteration depth, or hits a detector. When a ray hits a detector, the phase of the ray at the centre of the detector is calculated* from the lengths of the parent rays and their local refractive indices. The phase difference between the rays that hit the two photodiodes is then converted to a measured displacement with eq. (2.4), which is also the equation used for data analysis in the real system.

Results. The approximate location and orientation of the optical components in the real setup was transferred into the simulation. For each component, small adjustments to position and orientation were made to determine how the measured distance changes with the movement of the component. In Table 3.2, the sensitivity of each optical component to translation and rotation is shown, for both the one-mirror setup and the three-mirror setup.

---

*The detectors are assumed to be ideal and pointlike, in order to avoid the computational cost of integrating an interference pattern over a detector with finite area. Thus, the simulated systems always operates at maximum contrast.

(a) Setup with one reference mirror.

Component	Sensitivity to					
	translation (nm/nm)			rotation (nm/μrad)		
	x	y	z	x	y	z
M1	0	0	0	0	0	0
BS1	0	0	0	0	0	0.240
AOM1	0	0	0	0	0	0
AOM2	0	0	0	0	0	0
M2	0	0	0	0	0	0.240
M3	0	0	0	0.006	0.006	0.240
M4	0	0	0	0.006	0.006	0.240
BS2	0	0	0	7.002	0	0.001
PBS1	0	0	0	0	0	0
QWP1	0	0	0	0	0	0
M5	0	0	0	0	0	0.001
M6	–	–	–	–	–	–
M7	–	–	–	–	–	–
BS3	0	0	0	0	7.002	0.001
PD1	0	0	0	0.005	0	0
PD2	0	0	0	0.005	0	0

(b) Setup with one reference mirror and two measurement mirrors.

	Sensitivity to					
	translation (nm/nm)			rotation (nm/μrad)		
	x	y	z	x	y	z
M1	0	0	0	0	0	0
BS1	0	0	0	0	0	0.240
AOM1	0	0	0	0	0	0
AOM2	0	0	0	0	0	0
M2	0	0	0	0	0	0.240
M3	0	0	0	0.006	0.006	0.240
M4	0	0	0	0.006	0.006	0.240
BS2	0	0	0	7.002	0	0
PBS1	0	0	0	0	0	0
QWP1	0	0	0	0	0	0
M5	0	0	0	0	0	8.388
M6	1.000	0	0	0	149.386	0.315
M7	1.000	0	0	0	149.386	0.924
BS3	0	0	0	0	7.002	0.001
PD1	0	0	0	0.005	0	0
PD2	0	0	0	0.005	0	0

Table 3.2: Simulated sensitivity of the metrology distance measurement to position and orientation of the optical components in **(a)** the one-mirror setup and **(b)** the three-mirror setup. The component labels and coordinate axes are as in fig. 3.1. Values smaller than 10^{-3} are shown as 0. As expected from the analysis in section 2.3, the setup is resilient to changes in the position and orientation of optical components.

Component	Sensitivity to z-rotation (nm/µrad)		
	measured	simulated	
		ideal setup	1° misalignment
M3	0.18(9)	0.24	0.24
M5	0.045(23)	0.000 62	0.25

Table 3.3: Comparison of the simulated sensitivity from table 3.2 with measurements. Two simulations are shown: one with a perfectly aligned setup, and one where PBS1 was rotated by 1° around the z-axis from its ideal position, and then the simulated setup was aligned to accommodate for the change. The measurements agree with the simulation, but the simulated values for M5 depend strongly on the initial alignment.

As expected from the analysis in section 2.3, the metrology is resistant to changes in position of all components, with a sensitivity less than $5 \cdot 10^{-6}\,\mathrm{nm\,nm^{-1}}$, except for the measurement mirrors, which have the expected sensitivity of $1\,\mathrm{nm\,nm^{-1}}$. This serves as a confirmation of eq. (2.4), which is used in both the raytracer and the data analysis of the real setup.

In the one-mirror setup, BS2 and BS3 are most sensitive to rotation, and in the three mirror setup, the measurement mirrors M5 and M6 have the largest sensitivity, which is the expected effect of cosine error.

Comparison with measurements. Some of the simulated values in table 3.2 were compared with measured values. The mounts were rotated with adjustment screws by hand, and even small adjustments had a large influence on measured phase, contrast, and intensity. Thus, the uncertainty in the measurements is $\approx 50\,\%$, which may be an inaccurate estimate.

The results of the comparison between simulation and measurement are shown in table 3.3.

For M3, the measurement agrees with the simulation within the estimated uncertainty.

For M5, the result depends strongly on how exactly the components are set up. Rotating PBS1 in the simulation by 1° around the z-axis from its ideal* position, and then re-aligning the rest of the simulated setup to accommodate for the change, changes the simulated sensitivity by a factor of ≈ 300. The measurement agrees with the simulation within this range, but the uncertainty is large.

The sensitivity of the metrology to component rotation and translation is thus greatly influenced by how close the setup is to a perfectly aligned interferometer. An accurate initial placement and orientation of components is rewarded with a lower sensitivity to disturbances. Since the real metrology is

---

*The ideal setup is defined as the one in which all beams that are shown as perpendicular or parallel in fig. 3.1 are exactly perpendicular or parallel. This is hard to measure in the real setup, but easy to realize in the simulation.
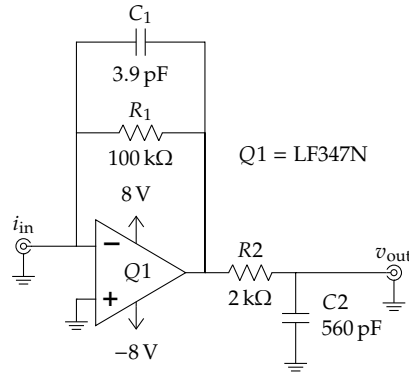
Figure 3.3: Schematic of the photodiode-amplifier. The input current is converted to a voltage by $Q1$ with transimpedance gain $R1$. The low-pass filter $R2\ C2$ has bandwidth $f_{-3\,\mathrm{dB}} \approx 150\,\mathrm{kHz}$.

set up by hand without measurement tools, deviations of the metrology from its simulation are expected.

3.4 Photodiode amplifier

Two identical photodiode amplifiers were built on a breadboard to convert the current from the photodiodes PD1 and PD2 to a voltage that can be measured with an oscilloscope. The schematic of the amplifier is shown in fig. 3.3.

The amplifier consists of a transimpedance amplifier with a gain of $v_{\mathrm{out}}/i_{\mathrm{in}} = 100\,\mathrm{k\Omega}$ and a low pass filter with $f_{-3\,\mathrm{dB}} \approx 150\,\mathrm{kHz}$. The phase noise of the amplifier was tested by connecting the current input of the amplifier to a function generator and a shunt resistor, and the voltage output of the amplifier to an oscilloscope. The two amplifiers were given the same input signal from the function generator, but with a constant phase offset. The phase difference was then measured on the oscilloscope and converted into a displacement according to eq. (2.4).

The time series and the periodogram of the noise are shown in fig. 3.4. The average standard deviation during the 2 s measurement was 0.022 nm, with a peak-to-peak noise of 0.28 nm. Over a 24 h period, the drift of the amplifier was less than 0.1 nm. This satisfies the requirement of 0.45 nm peak-to-peak noise for NICE.
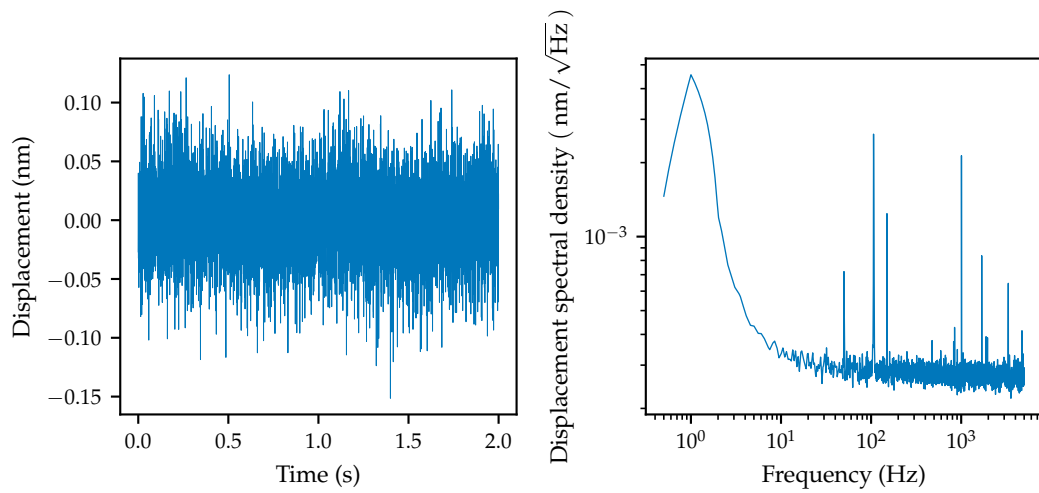
Figure 3.4: Noise of the measurement electronics during a 2 s measurement with 10 kHz sampling. The measurement signal was given by a signal generator instead of the photodiodes, in order to isolate the electronic noise from the metrology noise.

4 Results

Each description of an experiment in this chapter contains a short overview of the setup, the experimental results, and the discussion of the results.

In section 4.1, the distance measured by the metrology is compared to the distance measured by a calibrated linear piezo stage to determine how linear and accurate the metrology is.

The noise over short time periods is measured in section 4.2, and the long-term drift of the setup is measured in section 4.3.

Section 4.4 contains the measurements of the bandwidth of the metrology.

4.1 Linearity

Setup. The directly measured output of the metrology is a phase shift between two beat signals, which is converted into the mirror displacement with eq. (2.4). In order to confirm this theoretical result, one measurement mirror of the metrology was mounted on a calibrated closed-loop linear piezo stage. The mirror displacement measured by the metrology, $d_{\text{metrology}}$, and the mirror displacement measured by the optical encoder of the piezo stage, d_{piezo}, were recorded while a triangle wave was applied to the piezo stage.

Results. The displacement over time is shown in fig. 4.1, where one wave is offset slightly for better visualization. Both devices measure the triangle wave.

The difference between the distance measurement of the metrology and the piezo is shown in fig. 4.2. Over a displacement of $\approx 80\,\text{nm}$, the metrology deviates from the piezo by $\approx 4\,\text{nm}$. The deviation is linear in d_{piezo}. A Bayesian linear fit gives an error of

$$\frac{d_{\text{piezo}} - d_{\text{metrology}}}{d_{\text{piezo}}} = 0.050\,92(22).$$

Discussion. There are several sources of error that can account for the systematic discrepancy between the measurement of d_{piezo} and the measurement of $d_{\text{metrology}}$: cosine error in the alignment, uncertainty in the calibration of the piezo, and uncertainty in the measurement of the monitor signal of the piezo.
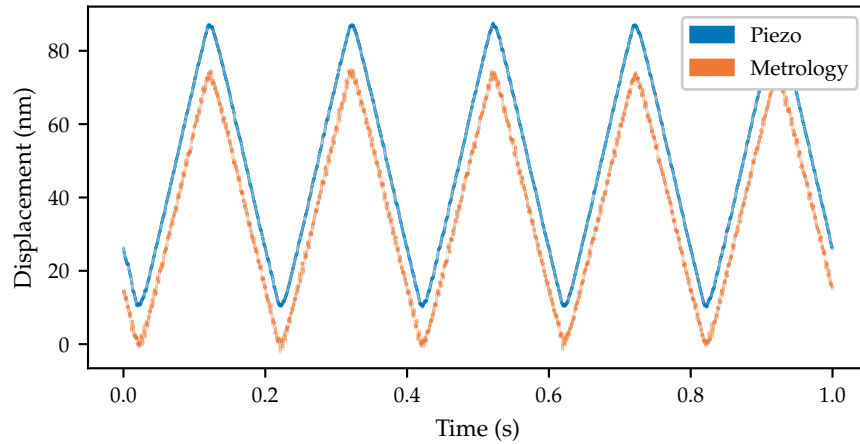
Figure 4.1: Comparison of distance measured by the optical encoder of the piezo and distance measured by the metrology, over time. The distance measured by the piezo is shifted up by 10 nm for better visibility. A triangle wave was applied to the piezo controller in order to determine the linearity of the metrology.
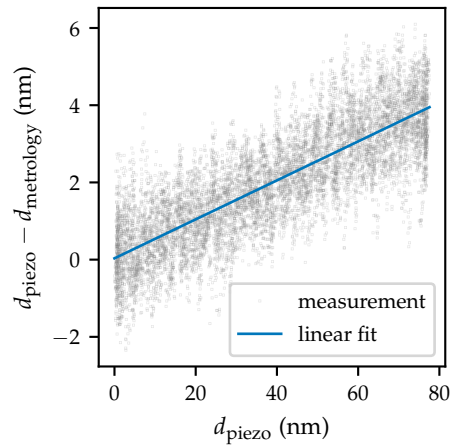
Figure 4.2: Difference between piezo measurement and metrology measurement as a function of distance. The independent measurement methods agree to within $\approx 5\%$, over a distance of 80 nm, and the deviation is linear.

If this error of $\approx 5\,\%$ were caused by cosine error, the misalignment would be $18.36(4)°$. This is larger than expected, because a misalignment by such a large angle should be visible by eye.

The uncertainty of the calibration of the piezo stage is not explicitly specified by the manufacturer, but the calibration constant is given with five significant digits,* which is too high an accuracy to account for a $5\,\%$ error.

The monitor voltage of the piezo was measured with an 8 bit ADC in an oscilloscope, with the signal at almost full scale. For the measurement of d_{piezo} near $80\,\text{nm}$, this can account for an error of up to $\approx 1/256 \approx 0.5\,\%$, which can not account for a $5\,\%$ measurement error.

These sources of error are all unlikely. If the deviation of $5\,\%$ is constant in time, it is not currently a major limitation of the metrology, and no further investigation was carried out.

4.2 Noise

Setup. To determine the noise floor of the metrology, only the internal reference mirror (M5, see fig. 3.1) was used to reflect all four beams. In the absence of all noise sources, the metrology should measure a constant phase, independent of the position of M5.

The metrology was initially placed on a piece of $3\,\text{cm}$ thick sponge foam on an undamped optical table, and later moved onto a platform on sorbothane feet on a damped optical table. Both setups are compared.

The phase was sampled at a frequency of $10\,\text{kHz}$ for $2\,\text{s}$ with an oscilloscope. The phase noise floor of the electronics is also shown for comparison. All periodograms are averages of ≈ 60 periodograms taken in immediate succession to reduce noise.†

Results. The phase over time in a randomly selected $2\,\text{s}$ measurement period for each setup is shown in fig. 4.3. The damped setup has significantly lower noise, with $0.8\,\text{nm}$ peak-to-peak, than the undamped setup with $2\,\text{nm}$ peak-to-peak.

The periodograms in fig. 4.4 show that the damped setup performs better than the undamped setup, and that the metrology is not limited by noise of the measurement electronics, except for three narrow peaks in the electronic noise.

All measured periodograms show flicker noise ($\mathcal{P} \propto 1/f$), white noise ($\mathcal{P} = \text{const.}$), and wide and narrow peaks.

The undamped setup shows vibrations at $\approx 50\,\text{Hz}$ and $\approx 30\,\text{Hz}$ which are reduced in the damped setup. These vibrations can be amplified by knocking on the optical table with various frequencies from $0.5\,\text{Hz}$ to $5\,\text{Hz}$, but the vibrations measured by the metrology are still dominated by $30\,\text{Hz}$ and $50\,\text{Hz}$.

---

*The datasheet of the piezo stage claims a resolution of $0.04\,\text{nm}$, and it was calibrated by the manufacturer to give a displacement of $31.066\,\text{µm}$ at $10\,\text{V}$ input.
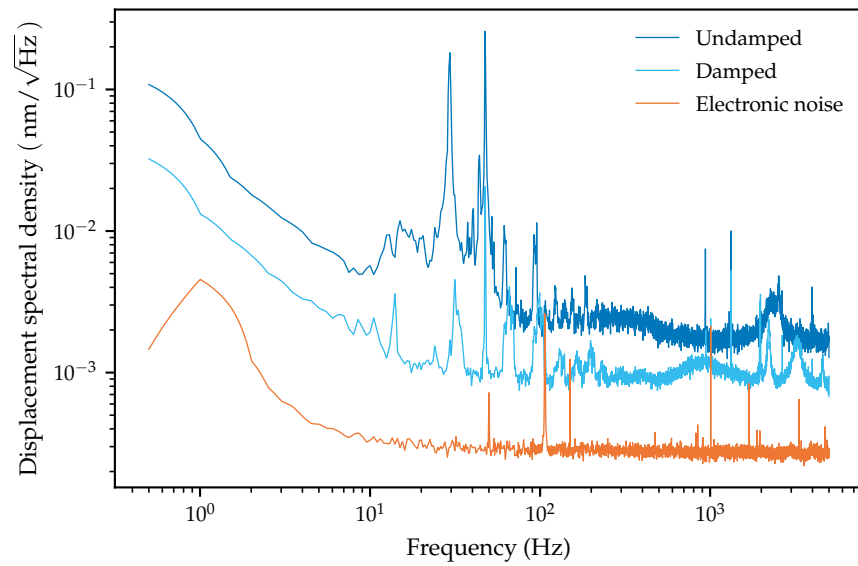
†For each time series, the periodogram was computed separately, and the resulting periodograms were averaged. This process is called Welch's method.
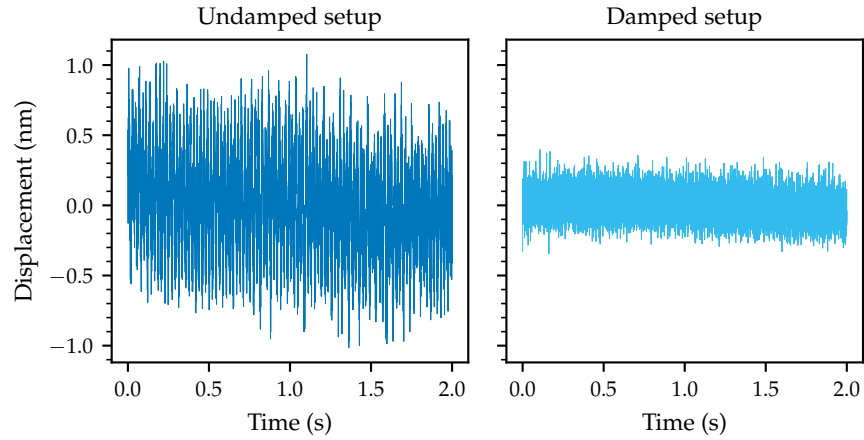
Figure 4.3: Displacement over time measured by the metrology with all four metrology beams reflected by the same stationary mirror. This is the noise floor of the metrology.

Figure 4.4: Periodogram of the measured metrology displacement with all four metrology beams reflected by the same stationary mirror. This is the noise floor of the metrology. The setup on the damped optical table and sorbothane feet performs better than the undamped setup, especially for vibration peaks in the 30 Hz and 50 Hz region.

Probability	Probable region width (nm)	
	Damped setup	Undamped setup
50 %	0.12	0.47
90 %	0.31	1.06
99 %	0.49	1.51
99.9 %	0.61	1.87
99.99 %	0.72	2.04
100 % (peak-to-peak)	0.74	2.09

Table 4.1: Statistics of the noise measurements of the damped and the undamped metrology. The width of the Bayesian probable region is given as a function of the probability. Conversely, this is also the percentage of samples that lie within a region of specified width. The damped setup outperforms the undamped setup by a factor of ≈ 3. The damped setup almost fulfils the requirements for NICE, with 0.8 nm peak-to-peak noise over 2 s.

Both the white noise and the $1/f$ noise of the metrology are improved by a factor of ≈ 3 by damping.

Some statistics of the measurements are shown in table 4.1. The damped setup has a peak-to-peak displacement noise of ≈ 0.8 nm over 2 s and is close to the NICE requirement of 0.45 nm peak-to-peak.

Discussion. The 30 Hz noise and the 50 Hz noise can be amplified by knocking on the table with lower frequencies, which may indicate that the frequencies are resonant frequencies of the metrology setup, and can be avoided by damping the setup. The sorbothane feet of the damped setup claim an absorption of 80 % to 100 % of vibrations that have frequencies of 50 Hz or higher, which agrees with the ≈ 10 times decrease of the peak in the periodogram.

The improvement in white noise could be explained by damping of vibrations by the sorbothane feet, which are most effective at frequencies higher than 50 Hz. The improvement in $1/f$ noise could be partially explained by the optical table, which dampens at least 96 % at frequencies of 10 Hz or higher, but this does not account for the improvement at even lower frequencies.

The effectiveness of the damping is highest in the region from 10 Hz to 100 Hz, which agrees with the specifications of the sorbothane feet and the damped optical table.

Integrated noise. From the periodogram, the contribution of noise in certain frequency ranges to the standard deviation of a measurement can be calculated with eq. (2.11).

Figure 4.5 shows what standard deviation of the noise can be expected as a function of measurement time. While the metrology can sample with a rate up to 10 kHz, the intended use in NICE as a closed-loop feedback system only requires a sampling rate of ≈ 100 Hz. When sampling at a slow rate, many measurements can be averaged to reduce the contribution of white noise to the
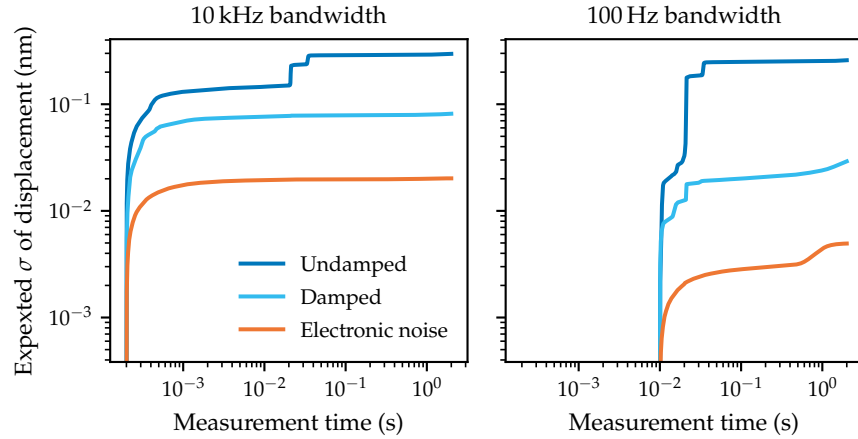
Figure 4.5: The expected standard deviation as a function of measurement time, for different sampling rates. These are the frequency-integrated periodograms of the displacement noise. When sampling with a 100 Hz bandwidth, the damped setup gives $\sigma \approx 30$ pm when measuring for 2 s.

uncertainty of the measurement. For this reason, the expected noise levels are shown for the full 10 kHz bandwidth and the slower 100 Hz bandwidth.

The contribution of 50 Hz and 30 Hz noise are clearly visible for the undamped setup, but are barely visible in the damped setup, which agrees with the periodogram in the previous section. Reducing the sampling rate to 100 Hz reduces the noise in the damped setup by a factor of ≈ 3, which gives an expected standard deviation of ≈ 30 pm.

At 100 Hz sampling, the noise is similar to the metrology by Clark,[6,11] at least for measurement times of a few seconds.

4.3 Drift

Setup. The same setup as in section 4.2 was used, but with measurements with a slower sampling rate of ≈ 1 Hz and over a longer time period of ≈ 40 h.

The air temperature near PBS1 was measured with a PT1000 probe attached to a multimeter via 4-wire sensing. The resistance of the probe was recorded only once per minute to avoid heating the probe with the measurement current.

Many experiments of this type were conducted with slight variations in the setup, such as location of the thermometer and size of the metrology box, but they all showed similar performance. Thus, only one is shown here.

Results. Phase and temperature over time are shown in fig. 4.6. The temperature changes by $\approx 0.7\,°C$ peak-to-peak, while the distance measurement drifts by ≈ 3.5 nm. The temperature seems slightly periodic in time, with peaks at
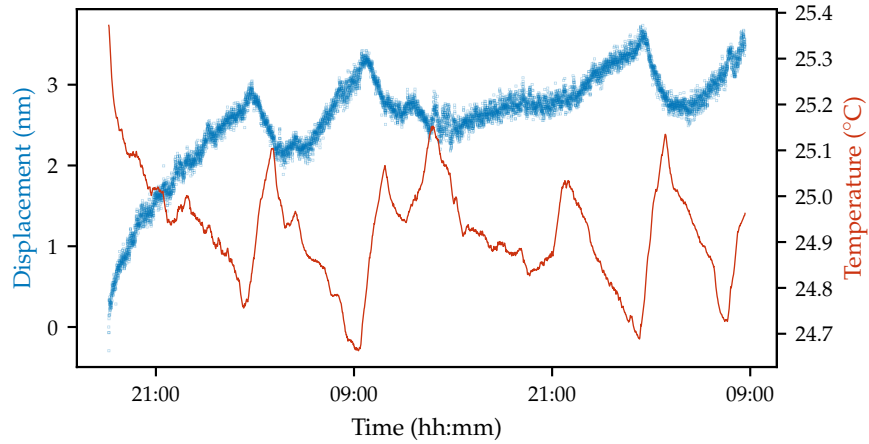
**Figure 4.6:** The metrology drifts by $\approx 3.5\,\text{nm}$ over a period of $\approx 40\,\text{h}$. The air temperature was measured close to PBS1, and shows some negative correlation during the first six hours of the experiment, but not later. Both temperature and displacement are somewhat periodic, with an $\approx 24\,\text{h}$ period.
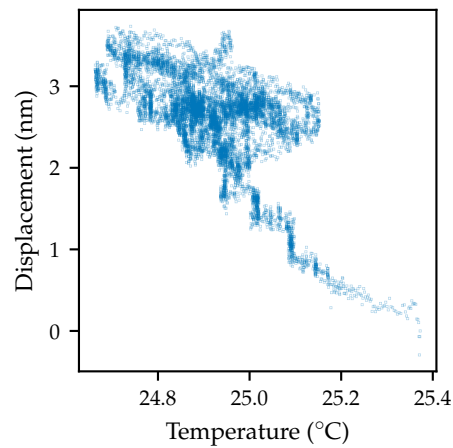
Figure 4.7: The correlation between air temperature and displacement from fig. 4.6 over the $\approx 40\,\text{h}$ measurement period. There is a negative correlation with a temperature coefficient of $\approx -5\,\text{nm}\,\text{K}^{-1}$ that is visible to during the first six hours of the experiment (trend from upper left to lower right of figure), but the correlation is weaker during the rest of the experiment (upper half).

33
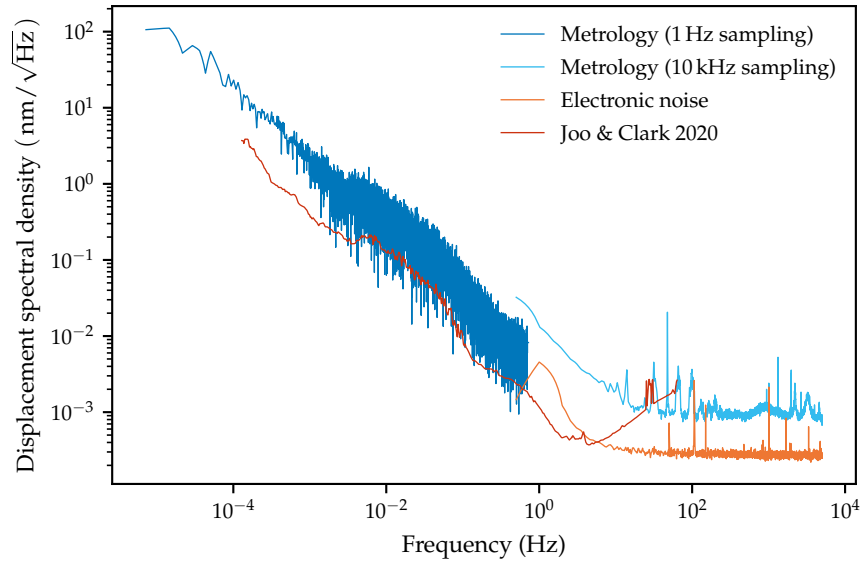
Figure 4.8: Periodogram of the metrology noise, with different sampling rates. The corner frequency between $1/f$ noise and white noise is at $\approx 10\,\text{Hz}$. The measurements with 1 Hz sampling rate and 10 kHz sampling rate do not line up well, which is explained in the main text.

similar times of day, which is probably caused by the programming of the air conditioning in the lab.

The correlation between phase and temperature is linear at the beginning, which is also visible in the correlation plot in fig. 4.7. After $\approx 6\,\text{h}$, the metrology drift stabilises slightly, and the correlation with temperature becomes much weaker. The thermal expansion coefficient during the first 6 h of the experiment is $\approx 4\,\text{nm}\,\text{K}^{-1}$, which is similar to the result obtained by Clark,[6,11] on which this metrology is based.

Excluding the first 6 h of the experiment, the metrology drifts by $\approx 1.5\,\text{nm}$ peak to peak.

Figure 4.8 shows an overview of all periodograms of the metrology, and compares it with the results obtained by Joo and Clark. During the drift test, the periodogram of the metrology approximately follows a power law with no visible periodic nonlinearity.

Discussion. The lack of correlation between temperature and measured displacement could be caused by a change in air pressure in the lab, which is estimated to have a similar effect on the metrology as temperature in section 3.2.2.

Additionally, one experiment was recorded where the correlation between phase and temperature was 99 % over a period of 40 h, but since the performance

in this experiment was not repeatable, it cannot be used to predict the behaviour of the metrology. However, this indicates that the environmental temperature can be the main source of drift of the metrology in some situations.

Active temperature control of the metrology is likely not a good option, since a temperature coefficient of $\approx 4\,\text{nm}\,\text{K}^{-1}$ requires a stabilisation of temperature better than $\approx 0.1\,\text{K}$ to fulfil the NICE requirements of $0.45\,\text{nm}$ peak-to-peak noise. This is difficult to realize for a box of size $\approx 50\,\text{cm} \times 30\,\text{cm} \times 30\,\text{cm}$. Since environmental conditions seem to be the main limitation of the metrology, a setup that is more compact or that operates at lower air pressure could improve the drift.

The periodogram from the drift test does not join up well with the periodogram from the high-frequency noise test. This is most likely due to the different oscilloscope used in the measurement, which has a less reliable phase detector that requires several averages to obtain a good phase reading. This should only affect the measurement at frequencies at around $1\,\text{Hz}$ to $0.1\,\text{Hz}$. Additionally, nobody was in the room during the drift measurements, which could potentially have reduced the noise caused by turbulence and air currents.

4.4 Bandwidth

Setup. The frequency response of the metrology was tested by actuating a calibrated piezo stage with a known frequency of $10\,\text{Hz}$, $100\,\text{Hz}$, or $1\,\text{kHz}$, and recording the metrology output.

The amplitude of the piezo actuation is $\approx 1.5\,\text{nm}$, but is not known accurately since the piezo monitor output voltage was too noisy. The monitor signal was thus measured with a multimeter in AC voltage mode in order to remove some of the noise, but the filtering process inherent in this measurement means that only the average peak-to-peak displacement of the piezo is known. Since this test is intended to measure to frequency response of the metrology, and the linearity and amplitude response were already determined in section 4.1, this is not a problem.

Results. The periodograms of the displacement are shown in fig. 4.9. For comparison, the noise floor of the metrology when no input is applied to the piezo is also shown. The vibrations appear at the correct frequency as sharp features in the spectrum. The setup has significant noise in the $100\,\text{Hz}$ to $1\,\text{kHz}$ region, which does not appear when only a single mirror reflects all beams, as in fig. 4.4.

Discussion. The metrology responds as expected to vibrations up to $1\,\text{kHz}$, which meets the bandwidth requirements for NICE of $100\,\text{Hz}$.

The additional noise, compared to a single-mirror setup, is most likely due to differential displacement between the two measurement mirrors. The increase in noise between $100\,\text{Hz}$ and $1\,\text{kHz}$ in the three-mirror setup could be acoustic, which would explain why it is not damped by the table.
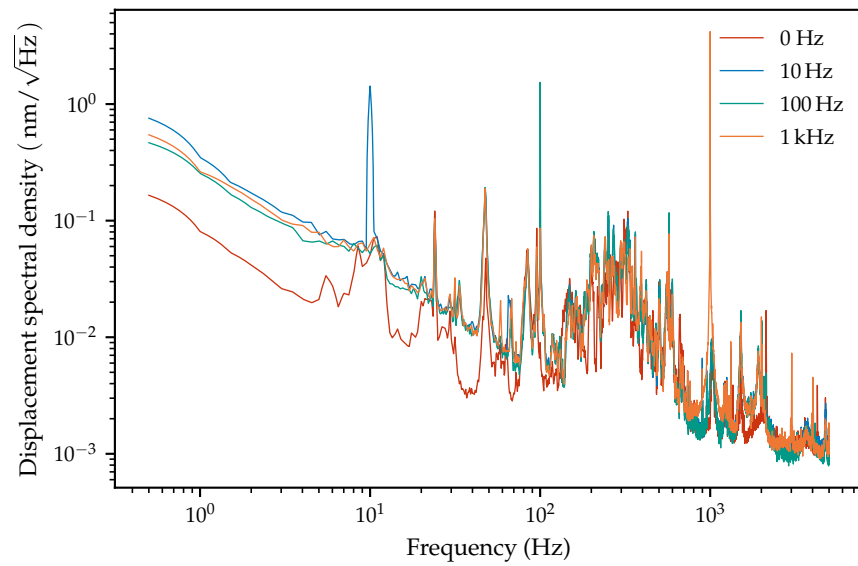
Figure 4.9: Periodogram of the metrology with one measurement mirror driven by a piezo actuator at different frequencies. Vibrations with frequencies of 10 Hz, 100 Hz, and 1 kHz, with an amplitude of ≈ 1.5 nm, were induced by the piezo. The 0 Hz periodogram corresponds to no input signal given to the piezo. The metrology shows the vibrations clearly, despite the presence of additional broad band noise ($f \approx 100$ Hz to 1 kHz) from the differential movement of the two separate measurement mirrors.

5 Conclusion

5.1   Methods and results

A heterodyne laser distance metrology based on the work of Joo[11] and Clark[6] was built and characterized for measuring optical path lengths in the upcoming Nulling Interferometry Cryogenic Experiment (NICE). The system operates at room pressure and temperature with a beat frequency of 10 kHz, and the optical path length difference between the two measurement mirrors is sampled with a frequency of 10 kHz.

The distance measurement agrees with a calibrated linear piezo stage to within 5 %. The noise floor of the metrology is a peak-to-peak mirror displacement of 0.74 nm over a measurement time of 2 s, and a drift of ≈ 4 nm over a measurement time of ≈ 40 h. The drift occasionally shows a 99 % correlation with temperature, but is usually not significantly correlated with temperature. The thermal expansion coefficient of this correlation is ≈ 4 nm K^{-1}.

5.2   Comparison with model

From the theoretical model of the metrology, a standard deviation of the drift of ≈ 4 nm to 40 nm was expected due to fluctuations of temperature and pressure in the lab. The measured peak-to-peak drift of ≈ 4 nm is better than expected from the model, which can be explained by better than expected matching of the optical path length differences within the metrology.

The noise of the metrology over short periods of 2 s is probably dominated by vibrations of the setup, which was not part of the theoretical model. Damping the metrology with a passively damped optical table and sorbothane feet has reduced the noise by a factor of ≈ 3, from 2.09 nm peak-to-peak to 0.74 nm peak-to-peak. The power spectrum still shows distinct peaks at frequencies of ≈ 20 Hz and ≈ 50 Hz, which are believed to be resonant frequencies of the setup.

As expected from simulations, there is no indication that thermal expansion of the optical table has an influence on the measurement, since the drift can be explained by changes in the refractive index of air. This confirms that the metrology is resilient to small changes in position of the optical components.

5.3 Comparison with NICE requirements

The preliminary bandwidth requirement of NICE of 100 Hz was met by the 10 kHz sampling rate of the metrology.

The requirement of 0.45 nm peak-to-peak noise was not met, which is due to vibrations of 0.74 nm peak-to-peak of the setup over short timescales, and drift of ≈ 4 nm over a timescale of 40 h.

The short-term noise can be reduced by averaging the samples from the 10 kHz sampling rate of the metrology to the required 100 Hz bandwidth. This reduces the standard deviation of the displacement measurement by a factor of 3, down to $\sigma \approx 30$ pm, which is still dominated by 20 Hz and 50 Hz vibrations of the components in the metrology.

The drift can be explained by fluctuations in temperature and pressure, both over time and over the large volume of the metrology box. In order to meet the long-term stability requirements of NICE, improvements have to be made.

5.4 Potential improvements

The possible improvements to the setup are categorized into those affecting short-term noise in section 5.4.1, and those affecting long-term drift in section 5.4.2.

5.4.1 Short-term noise.

For short time periods, vibrations of the optical setup are the dominant source of noise. This can be improved by better damping of the system, both against vibrations of the floor and vibrations that are transmitted by air. This can be realized by putting the setup onto an optical table with better damping, and building a metrology box that is soundproof. Alternatively, the setup could be changed so that it is resonant mostly at frequencies higher than 100 Hz, such that the influence of resonant vibrations can be averaged out.

Additionally, for the higher attenuation that is expected from NICE, and the resulting lower intensity of the laser beam at the photodiodes, electronic noise will at some point be a significant contribution. Better photodiode amplifiers thus have to be used for measurements at high attenuation.

5.4.2 Long-term drift.

Over long measurement times, temperature and pressure changes over time and position in the setup are believed to be the dominant source of noise. Many possible methods to reduce this drift of the setup exist, and they are described here in order of ascending effort.

Temperature and pressure measurements. Pressure and temperature of the air in the setup can be measured at multiple points to determine how these parameters vary over time and position. These measurements could provide

clues as to how the setup is influenced by environmental conditions, and the data could possibly be used to reliably detrend the distance measured by the metrology over long time periods.

This approach is promising, since a 99 % correlation of temperature and measured distance was recorded over a period of two days, but the experiment was unfortunately not repeatable. This shows that, in principle, such an approach is viable, but closer investigations are needed.

Isolating the AOMS from the metrology. Currently, the acousto-optic modulators, which are necessary for shifting the frequency of the laser, are placed in the same box as the metrology interferometer. The AOMS generate $\approx 1\,\mathrm{W}$ of heat, which is transported away by natural air convection. This produces air currents, temperature inequalities, and turbulence in the setup, which makes the detrending described above difficult, since temperature measurements at multiple locations might be necessary. Isolating the AOMS, which are the only significant heat source in the metrology box, could facilitate detrending and reduce turbulence and air currents in the setup.

Miniaturization and precision placement. Reducing the size of the metrology and using precision techniques to position the components would have an influence on multiple noise sources.

First, the sensitivity of the metrology to changes in refractive index of air are caused by not exactly matching the optical path lengths after BS2 in the setup. Reducing the size of the setup and using precision techniques to place the components will reduce the optical path length mismatch, in turn reducing the thermal expansion coefficient, and thus make the metrology more resilient to temperature and pressure changes.

Second, in a smaller volume, differences in air temperature and pressure tend to equalize quicker, and the setup can be closer to thermal equilibrium. This would simplify the strategy in the first approach to measure temperature and pressure in the setup.

Third, the largest possible modes of turbulence in the setup would be smaller, and the amount of turbulence and air currents that disturb the measurement would be reduced. This could improve noise over timescales of seconds to minutes.

Fourth, damping of the setup would be easier, since the resonant frequencies of smaller components tend to be higher, and a small and light setup is easier to isolate from the environment in a solid soundproof box.

Active control of the environment. With a thermal expansion coefficient of $\approx 4\,\mathrm{nm\,K^{-1}}$ in a box with large dimensions, $\approx 50\,\mathrm{cm} \times 30\,\mathrm{cm} \times 30\,\mathrm{cm}$, as measured for the current setup, active temperature control is a difficult task. However, with the smaller box proposed above, the volume to be controlled would be smaller, which would enable tighter control of the environmental conditions. Also, with the closer matching of optical path length differences that

would go with miniaturization, the thermal expansion coefficient is expected to be smaller.

Low-pressure environment. Reducing the air pressure in the metrology reduces the influence of air temperature and pressure variations on the measured distance, effectively reducing the thermal expansion coefficient. Additionally, turbulence and air currents would have a reduced effect on the measurements. This approach requires a major redesign of the setup, since none of the components currently used are vacuum rated. Reducing the environment to a near vacuum would eliminate all potential sources of drift that are currently limiting the setup.

Bibliography

1. Michael Bass et al. *Handbook of Optics, Volume I: Geometrical and Physical Optics, Polarized Light, Components and Instruments*. 3rd Edition. McGraw Hill Professional, 2009.

2. Max Born and Emil Wolf. *Principles of Optics*. 60th Edition. Cambridge University Press, 2019.

3. W. L. Bragg. "The diffraction of short electromagnetic waves by a crystal." In: *Proceedings of the Cambridge Philosophical Society* 17 (1914), pp. 43–57.

4. James Carvill. *Mechanical Engineer's Data Handbook*. 1st Edition. Elsevier, 2012.

5. Philip E. Ciddor. "Refractive index of air: new equations for the visible and near infrared". In: *Applied Optics* 35.9 (1996), pp. 1566–1573. DOI: 10.1364/AO.35.001566.

6. Erin Clark. "Compact heterodyne interferometer for high precision displacement measurements". Master thesis. University of Arizona, 2020.

7. LIFE collaboration et al. "Large Interferometer For Exoplanets (LIFE): I. Improved exoplanet detection yield estimates for a large mid-infrared space-interferometer mission". In: *arXiv:2101.07500 [astro-ph]* (2021).

8. P. Debye and F. W. Sears. "On the Scattering of Light by Supersonic Waves". In: *Proceedings of the National Academy of Sciences* 18.6 (1932), pp. 409–414. DOI: 10.1073/pnas.18.6.409.

9. Viktor Enfeldt. "Real-Time Ray Tracing With Polarization Parameters". Master thesis. Karlskrona, Sweden: Blekinge Institute of Technology, 2020.

10. Adrian A. Gheorghe et al. "Preparatory studies for a mid-infrared nulling interferometry experiment at cryogenic conditions". In: *Optical and Infrared Interferometry and Imaging VII*. Vol. 11446. SPIE, pp. 586–594. DOI: 10.1117/12.2576326.

11. Ki-Nam Joo et al. "A compact high-precision periodic-error-free heterodyne interferometer". In: *Journal of the Optical Society of America A* 37.9 (2020), B11. DOI: 10.1364/JOSAA.396298.

12. Charles Kittel. *Introduction to Solid State Physics*. 8th Edition. Wiley, 2004.

13. Adrian Korpel. *Acousto-Optics*. 2nd Edition. CRC Press, 1996.

14. Enbang Li et al. "Optical phase shifting with acousto-optic devices". In: *Optics Letters* 30.2 (2005), pp. 189–191. DOI: 10.1364/OL.30.000189.

15. René Lucas and Pierre Biquard. "Propriétés optiques des milieux solides et liquides soumis aux vibrations élastiques ultra sonores". In: *Journal de Physique et le Radium* 3.10 (1932), pp. 464–477. DOI: 10.1051/jphysrad:01932003010046400.

16. Scott L Miller and Donald Childers. *Probability and random processes: with applications to signal processing and communications*. 2nd Edition. Elsevier, 2012.

17. D. T. Pierce and R. L. Byer. "Experiments on the Interaction of Light and Sound for the Advanced Laboratory". In: *American Journal of Physics* 41.3 (1973), pp. 314–325. DOI: 10.1119/1.1987217.

18. Sascha P. Quanz et al. "Atmospheric characterization of terrestrial exoplanets in the mid-infrared: biosignatures, habitability, and diversity". In: *Experimental Astronomy* (2021). DOI: 10.1007/s10686-021-09791-z.

19. C. V. Raman and N. S. Nagendra Nathe. "The diffraction of light by high frequency sound waves: Part I." In: *Proceedings of the Indian Academy of Sciences - Section A* 2.4 (1935), pp. 406–412. DOI: 10.1007/BF03035840.

20. Thilo Schuldt et al. "Sub-Nanometer Heterodyne Interferometry and Its Application in Dilatometry and Industrial Metrology". In: *International Journal of Optomechatronics* 3.3 (2009), pp. 187–200. DOI: 10.1080/15599610903144153.

21. René Schödel. *Modern Interferometry for Length Metrology: Exploring limits and novel techniques*. 1st Edition. IOP, 2018.

22. Eugene Serabyn. "Nulling interferometry: symmetry requirements and experimental results". In: *Interferometry in Optical Astronomy*. Vol. 4006. SPIE, 2000, pp. 328–339. DOI: 10.1117/12.390223.

23. *Thorlabs HRS015B Stabilized Red HeNe Laser*. URL: https://www.thorlabs.com/newgrouppage9.cfm?objectgroup_id=5281 (Accessed: 09/14/2021).

List of Figures

List of Tables